Remote sensing of surface pressure on Mars with the Mars Express/OMEGA spectrometer: 2. Meteorological maps

Aymeric Spiga, François Forget, Bastien Dolla, Sandrine Vinatier, Riccardo Melchiorri, Pierre Drossart, Aline Gendrin, Jean-Pierre Bibring, Yves Langevin, Brigitte Gondet

Remote sensing of surface pressure on Mars with the Mars Express/OMEGA spectrometer: 2. Meteorological maps

Aymeric Spiga,[1] François Forget,[1] Bastien Dolla,[1] Sandrine Vinatier,[2] Riccardo Melchiorri,[2] Pierre Drossart,[2] Aline Gendrin,[3] Jean-Pierre Bibring,[3] Yves Langevin,[3] and Brigitte Gondet[3]

Received 28 November 2006; revised 6 July 2007; accepted 7 August 2007; published 30 August 2007.

[1] Surface pressure measurements help to achieve a better understanding of the main dynamical phenomena occurring in the atmosphere of a planet. The use of the Mars Express OMEGA visible and near-IR imaging spectrometer allows us to tentatively perform an unprecedented remote sensing measurement of Martian surface pressure. OMEGA reflectances in the CO_2 absorption band at 2 μm are used to retrieve a hydrostatic estimation of surface pressure (see companion paper by Forget et al. (2007)) with a precision sufficient to draw maps of this field and thus analyze meteorological events in the Martian atmosphere. Prior to any meteorological analysis, OMEGA observations have to pass quality controls on insolation and albedo conditions, atmosphere dust opacity, and occurrence of water ice clouds and frosts. For the selected observations, registration shifts with the MOLA reference are corrected. ''Sea-level'' surface pressure reduction is then carried out in order to remove the topographical component of the surface pressure field. Three main phenomena are observed in the resulting OMEGA surface pressure maps: horizontal pressure gradients, atmospheric oscillations, and pressure perturbations in the vicinity of topographical obstacles. The observed pressure oscillations are identified as possible signatures of phenomena such as inertia-gravity waves or convective rolls. The pressure perturbations detected around the Martian hills and craters may be the signatures of complex interactions between an incoming flow and topographical obstacles. Highly idealized mesoscale simulations using the WRF model enable a preliminary study of these complex interactions, but more realistic mesoscale simulations are necessary. The maps provide valuable insights for future synoptic and mesoscale modeling, which will in turn help in the interpretation of observations.

Citation: Spiga, A., F. Forget, B. Dolla, S. Vinatier, R. Melchiorri, P. Drossart, A. Gendrin, J.-P. Bibring, Y. Langevin, and B. Gondet (2007), Remote sensing of surface pressure on Mars with the Mars Express/OMEGA spectrometer: 2. Meteorological maps, *J. Geophys. Res.*, *112*, E08S16, doi:10.1029/2006JE002870.

1. Introduction

[2] Observing and analyzing the variations of atmospheric pressure on the surface of a planet is essential to understand the dynamics of its atmosphere. The first in situ ground pressure measurement on Mars, performed by the Viking Landers thirty years ago, revealed key Martian meteorological features [*Hess et al.*, 1980]. Later, the Pathfinder pressure sensor measurements yielded more insights on large-scale and regional meteorological phenomena [*Schofield et al.*, 1997].

[3] Mesoscale modeling studies, conducted to select appropriate landing sites for the Mars Exploration Rovers [*Rafkin and Michaels*, 2003; *Toigo and Richardson*, 2003], however, pointed out the scarce spatial and temporal coverage of the actual in situ meteorological measurements. This is especially true in the case of the surface pressure. Ideally, an alternative solution would be the remote measurement of surface pressure from orbit, as is done for temperature or water vapor [*Smith*, 2006].

[4] Surface pressure can be retrieved from the atmospheric IR spectra, using the linear correlation between the surface pressure and the CO_2 absorption band at 2 μm [*Gray*, 1966]. The feasibility of remote sensing measurements of surface pressure on Mars was examined in *Rosenqvist* [1991] and *Bibring et al.* [1991], and carried out with the spectral data from the imaging spectrometer ISM on the Phobos-2 mission. In a companion paper, *Forget et al.* [2007] describe a new and efficient remote sensing method to retrieve the

[1] Laboratoire de Météorologie Dynamique, Institut Pierre-Simon Laplace, Paris, France.
[2] LESIA, Observatoire de Paris, Meudon, France.
[3] Institut d'Astrophysique Spatiale, Orsay, France.

0148-0227/07/2006JE002870

surface pressure on Mars using the Mars Express/OMEGA visible and near-IR mapping spectrometer data set [*Bibring et al.*, 2004]. The surface pressure values retrieved from the OMEGA 2 μm band spectra are known with a relative 1-σ relative error around 7 Pa in bright regions and about 10 Pa in darker regions. The absolute accuracy of the pressure measurements (i.e., the systematic uncertainty on a whole given OMEGA session) is below 4%.

[5] The present paper is focused on the surface pressure maps obtained from these OMEGA observations and their use for a dynamical analysis of the Martian lower atmosphere. Using the ISM data sets, *Gendrin et al.* [2003] were able to produce maps with a resolution of ~25 km per pixel and identify pressure variations above Martian volcanoes and lee vortices. The present work can be considered as the continuation of the *Gendrin et al.* [2003] article, with a much better spectral and spatial resolution.

[6] "Surface pressure" for Mars should be precisely defined. CO_2 remote sensing retrievals are only atmospheric column mass estimations, i.e., hydrostatic surface pressure π_s measurements. These pressure measurements cannot be rigorously compared to ground-based barometer measurements, which feature the additional contribution from the atmospheric vertical motions. Following *Janjic et al.* [2001], and using the Laprise generalized vertical coordinates σ' [*Laprise*, 1992], the barometric non-hydrostatic surface pressure p_s can be expressed as:

$$p_s = \int_0^1 (1+\epsilon)\ \pi(\sigma')\ d\sigma' = \pi_s + \int_0^1 \epsilon\pi(\sigma')\ d\sigma' \qquad (1)$$

where π is the hydrostatic pressure at each layer σ' and ϵ is the ratio $\frac{1}{g}\frac{dw}{dt}$, which is non negligible when non-hydrostatic vertical motions become significant (g is the gravity acceleration and w the vertical wind component). Given the OMEGA horizontal resolution reaching the kilometer scale, we have to keep in mind the possibility that the hydrostatic pressure π_s measured by the instrument differs from the pressure p_s measured by a barometer at the surface of Mars, due to the non-hydrostatic vertical motions in the atmosphere.

[7] Beyond their interest for Mars atmosphere dynamics, the OMEGA surface pressure maps could provide relevant information for atmospheric science in general. Indeed, remote sensing surface pressure mapping seems far more difficult to achieve on Earth [*Mitchell and O'Brien*, 1987] than on Mars, and the main efforts on the remote CO_2 column measurements are more useful for quantifying carbon sources and sinks [*Buchwitz et al.*, 2006; *Bösch et al.*, 2006] and monitoring clouds [*Dubuisson et al.*, 2001; *Fournier et al.*, 2006] than extracting the pressure signal.

[8] The present work will also help to constrain Martian meteorological models with a better accuracy. General circulation models may benefit from inputs and diagnostics derived from the maps. Mesoscale models also need additional inputs, should they be qualitative signatures of the key mesoscale events on the surface pressure field (the equivalent of the dust cloud signature in the *Rafkin et al.* [2002] study) or quantitative estimates of surface pressure variations (the equivalent of the Pathfinder meteorological data used by *Tyler et al.* [2002]).

[9] Section 2 summarizes the background information on which the data processing used to obtain the surface pressure maps is based. Section 3 deals with the extraction of the meteorological signal from these surface pressure maps. Section 4 describes several examples of meteorological maps, and for each event, one or two plausible interpretations of the observed features are proposed.

2. Data Processing

2.1. A First Selection of the OMEGA Observations

[10] The Mars Express/OMEGA visible and near-IR mapping spectrometer characteristics and the pressure measurement method are detailed in the companion paper by *Forget et al.* [2007]. The OMEGA data set is extensive with nearly 4,000 nadir observations after more than one Martian year of acquisition phase. In general, there are distinct OMEGA "observations" (or "sessions" or "cubes") for the same Mars Express orbit [*Langevin*, 2005], as the scan length is modified depending on the spacecraft altitude (16, 32, 64, or 128 pixels). The horizontal resolution of the spectral images thus ranges from 5 km (scan length of 128 pixels) to ~400 m (scan length of 16 pixels, when surface was observed near-periapsis).

[11] Every OMEGA observation is potentially interesting and may be used for surface pressure retrieval. The following observation conditions are, however, problematic: very dark surfaces (for which Lambertian albedo $A_L < 0.1$); high solar zenith angle (i.e., insufficiently insolated regions with $\cos(i) < 0.6$); high reflectance values (saturation effects if $DN > 1200$); and high topography areas ($P_s < 150$ Pa).

2.2. Water Ice Biases

[12] The presence of water ice (IR absorber) in the atmosphere (clouds) or on the ground (frost) can distort the 2 micron CO_2 absorption band [*Gondet et al.*, 2006] and thus falsify the pressure retrieval. This is one of the reasons why the pressure retrieval is often meaningless in the polar regions. Fortunately, the wide OMEGA spectral coverage features the main water ice absorption bands, and allows the detection of ice in the atmosphere or on the ground [*Langevin et al.*, 2005; *Gondet et al.*, 2006]. In this paper, any pixel suspected to be contaminated by ice was rejected.

[13] A first check is done in the visible channel by taking advantage of the higher water ice cloud reflectivity in the blue compared to in the red. The method is similar to the one developed by *Wang and Ingersoll* [2002], and $\frac{blue}{blue+red}$ ratio maps are computed (Figure 1, left). This preliminary check is completed by a diagnostic of the H_2O absorption band at 1.5 μm. Band depth maps are built as shown on Figure 1 (right). In this example, water ice clouds are detected in the Elyseum Mons region.

[14] The presence of hydrated minerals may also affect the surface pressure measurement, due to the 1.91–1.93 micron signature. The locations where hydrated minerals are detected by OMEGA [see *Bibring et al.*, 2005, Figure 3] are thus avoided in this paper.

2.3. Influence of Atmospheric Parameters

[15] Once the above-mentioned limitations are taken into account, the surface pressure retrieval algorithm can be applied to the selected OMEGA sessions. As was shown

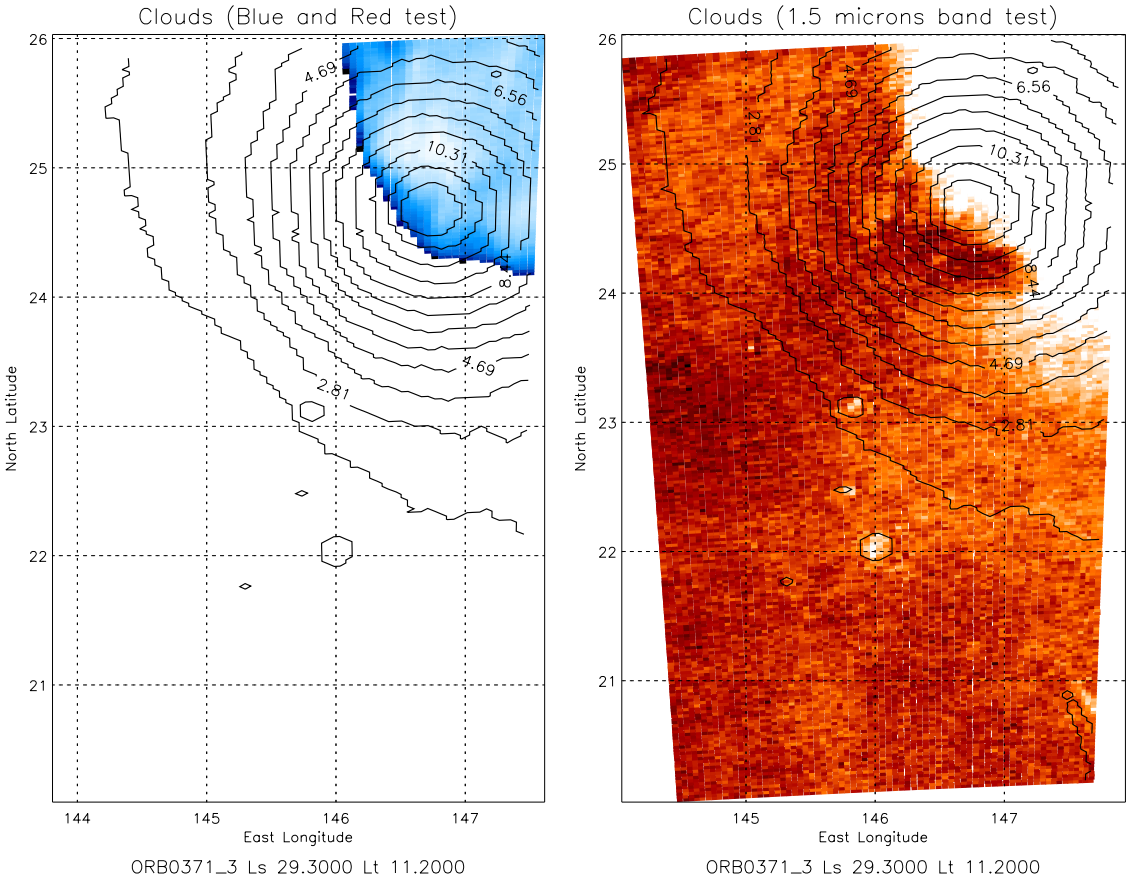

Figure 1. OMEGA water ice diagnostic in the Elyseum Mons region, at the beginning of spring, toward the end of the morning. Contours stand for the topography. (left) Visible test: blue reflectivity ratio with (blue + red) reflectivity. Clouds are found in the blue zones of the map. Blank pixels mean no water ice clouds are found. (right) The 1.5 μm band test: water ice absorption band ratio with the continuum. Clouds or frosts are found in the white zones of the map. Red and dark pixels mean no water ice clouds or frosts.

in the companion paper, the two main biases come from the uncertainties in the atmospheric parameters prescribed in the retrieval process, namely temperature profiles and dust opacity. These parameters are known from spatial and temporal interpolations of the Mars Climate Database (MCD) v4.1 large-scale fields [*Forget et al.*, 2006] derived from General Circulation Model (GCM) simulations. These are clearly irrelevant in the case of a peculiar mesoscale atmospheric event in the region, an unresolved local thermal contrast, or an unexpected local dust loading.

2.3.1. Dust Opacity

[16] In our inversion algorithm, the error induced by dust becomes significant for optical depth larger than 0.4. The TES dust column climatology retrieved in 2000–2001 enables a first raw selection of the OMEGA observations. In addition, the presence of atmospheric dust is checked qualitatively (Figure 2) with true-color images built with the OMEGA visible channel [*Bellucci et al.*, 2006]. Dust plumes can be identified in such visible maps, and the corresponding OMEGA session is then eliminated if the regions of predominant dust loading are too extensive.

2.3.2. Temperature

[17] In regions where topographical contrasts are dramatic, the spatial variability of afternoon temperatures may be particularly large [*Rafkin et al.*, 2001]. Atmospheric temperature discrepancies with the large-scale estimates are difficult to assess; however, the surface temperature field can be derived from the thermal part of the OMEGA spectra [*Jouglet et al.*, 2007]. Although on Mars the surface temperature is rather decorrelated from the atmospheric temperature, except in the lowest levels of the atmosphere, a comparison of the OMEGA surface temperature and the MCD estimates is useful to determine the unresolved radiative forcings. For example, insolation effects on the topographical slopes might lead to significant surface temperature excursions [*Rafkin et al.*, 2002; *Michaels et al.*, 2006]. On the insolated slopes, the temperature values from large-scale estimates are underestimated, which leads the retrieval algorithm to overestimate the measured pressure values, and the situation is reversed on shadowed slopes. In the present paper, the OMEGA sessions chosen in cratered terrains feature these surface temperature excursions, but differences are below ~10 K. The maximum limit for pressure bias is thus ~10 Pa, according to the sensitivity study done in the companion paper. In most observations, especially in flat areas, the OMEGA surface temperature measurements and the GCM surface temperature predic-

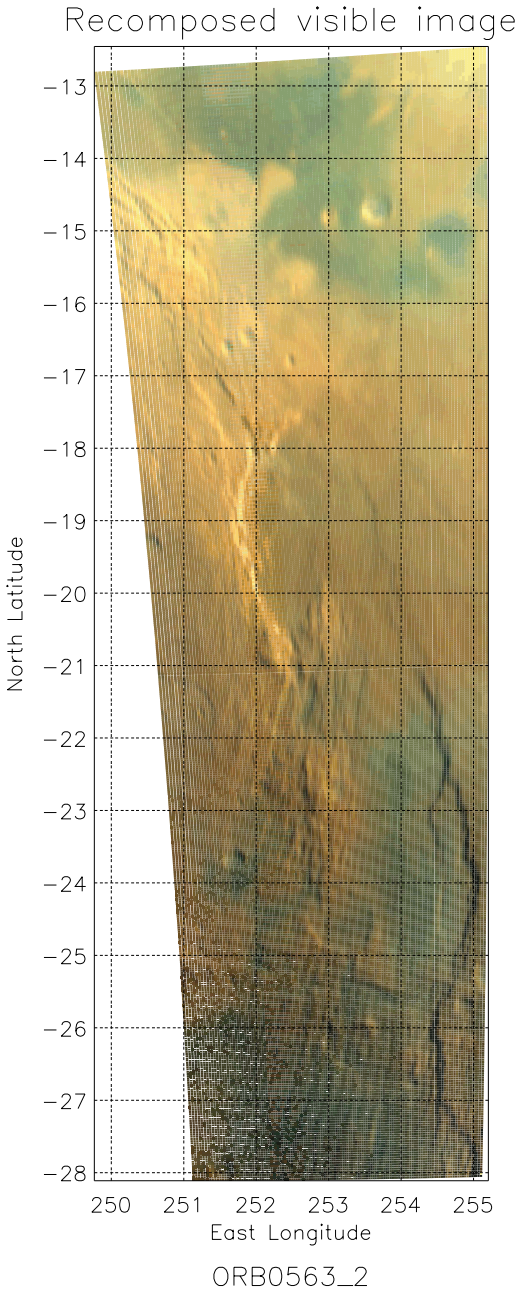

Figure 2. OMEGA recomposed true-color visible images of the Martian surface: case of a very clear atmosphere east of Solis Planum and west of Daedelia Planum.

tions are very close, resulting in much lower biases in the surface pressure measurement.

3. Extraction of the Meteorological Signal

3.1. Topographical Influence on the Surface Pressure Field

[18] Because hydrostatic surface pressure is a measurement of the quantity of gas in the atmospheric column above a given location, the field reaches its highest values in the depths of craters, and its lowest values at the summits of mountains. To first order, surface pressure maps are thus "images" of the planet's topography. This main influence is easily identified on the OMEGA 2 μm spectra, as shown in *Melchiorri et al.* [2006] and in the companion paper by *Forget et al.* [2007]. We give here an additional example in the southern hemisphere, in the Hellas basin. At the end of the southern hemisphere summer, the OMEGA instrument passed over a small crater feature at 48S,61E at the beginning of the afternoon. The dust storm activity during that year was moderate and the atmosphere not too loaded with dust. The OMEGA surface pressure measurement is given in Figure 3 (right). In comparison, Figure 3 (left) shows the surface pressure prediction (described in the companion paper and called in what follows P_{ref}) based on the reference MOLA 128 pixel per degree altimetry [*Smith et al.*, 2001].

3.2. Topography Removal

[19] In the present paper, the main objective is to analyze the meteorological signal in the OMEGA surface pressure maps. Therefore the first-order topographical contribution must be removed prior to any further analysis. A removal based on the transient properties of the main meteorological features (compared to the permanent surface pressure topographical contribution) is not possible here given the OMEGA spatial and temporal coverage. Another possibility, inspired from terrestrial meteorology, is "sea-level" pressure maps, which feature the meteorological depressions, anticyclones, ridges, troughs, and flat-flow areas. The sea-level reduction $P_{lev}(x, y)$ of the 2-D surface pressure field $P(x, y)$ is achieved by hydrostatic reduction of all the pressure values, using the altimetric inputs $z(x, y)$ from a Digital Terrain Model,

$$P_{lev}(x,y) = P(x,y)e^{-\int_{z(x,y)}^{z_{ref}} \frac{gdz'}{RT(x,y,z')}} \quad (2)$$

where z_{ref} is the altitude of reference that replaces "sea-level" on Mars, and R is the gas constant.

[20] Equation (2) requires a precise knowledge of the temperature profiles T. On Earth, the isothermal approximation is usually applied, which ensures in most cases a satisfying correction. On Mars, the choice of the right profile is not that straightforward. If we take an atmosphere lying above a surface with mountains and valleys, the objective is to define the right temperatures to use in equation (2) so that only pressure variations resulting from dynamical processes appear in the interpolated pressure fields. In particular, the leveled surface pressure field of a quiescent atmosphere should be constant.

[21] Similarly, we consider a theoretical slope on Mars on which no external dynamical process is acting. We assume a complete knowledge of the atmospheric thermal structure. The pressure at the top of the slope is reduced with equation (2) to the altitude at the bottom of the slope, by an integration between the two levels. The result should be equal to the pressure at the bottom of the slope. The integration in equation (2) can, however, take several paths: directly from top to bottom using the near surface air temperature; or, using a longer path, up, through the free atmosphere above the boundary layer, and then down. On Mars, in the afternoon, these two paths will yield very different results for the pressure at the bottom of the slope,

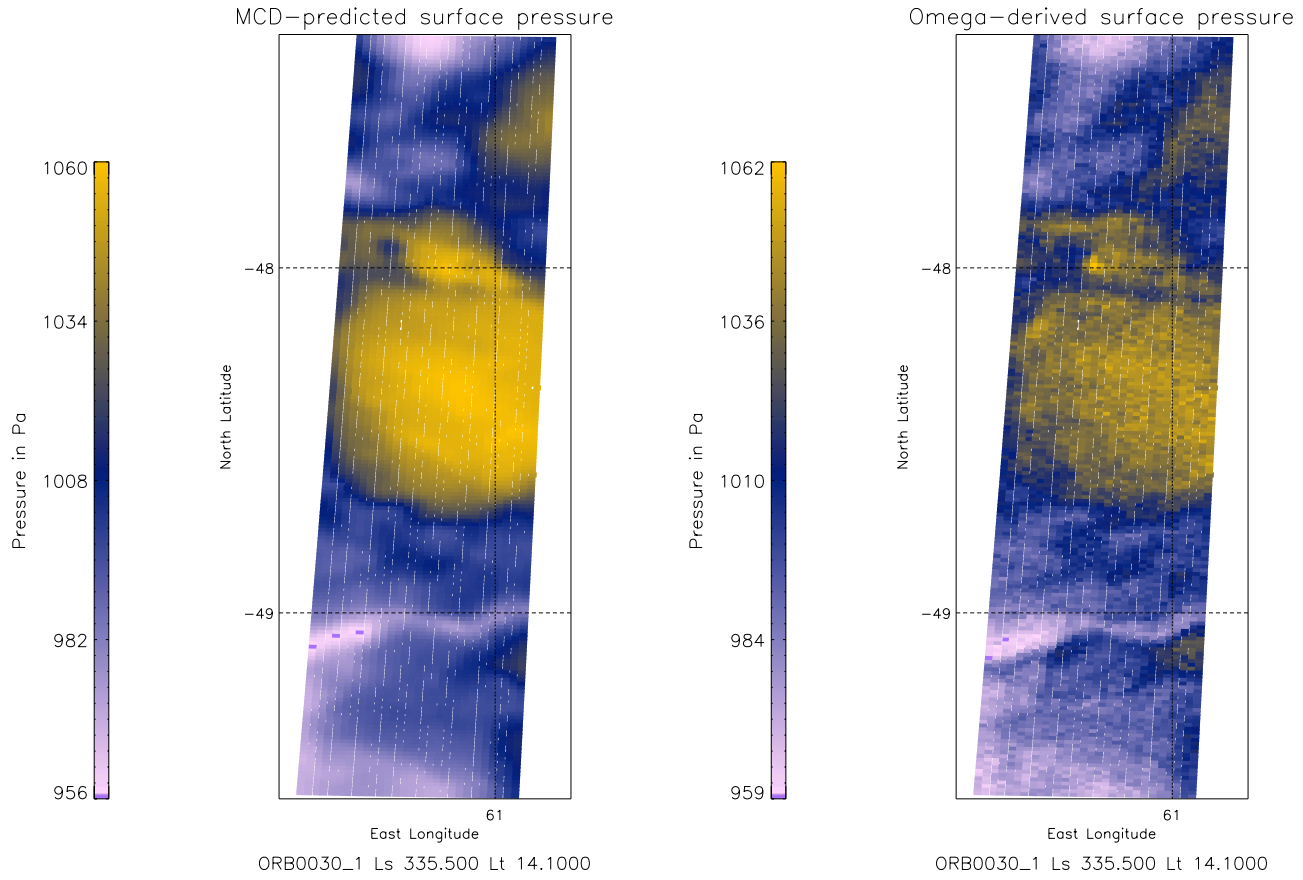

Figure 3. Surface pressure maps in the Hellas region. (left) Prediction based on the MOLA topography (see *Forget et al.* [2007] for details). (right) OMEGA remote sensing measurement. The residual noise on the pressure field is due to the degraded signal-to-noise ratio, as it is expected to occur on the low-albedo terrains of Hellas.

because the near-surface atmosphere is much warmer than the free atmosphere. Near the surface, the daytime heating by the ground necessarily induces buoyant forces that create upslope winds which violate the hydrostatic approximation. Thus the temperature of the isothermal approximation must be chosen high enough to be above the slope wind layer, but low enough to keep the above-mentioned "up" and "down" integration equivalent.

[22] On this basis, simulations using the LMD General Circulation Model fields were performed. It was found that by taking the air temperature at $\simeq$1 km above the surface, one could obtain maps of surface pressure interpolated to the zero datum free of topographical artifacts. In these maps, tidal and baroclinic waves are clearly identified, and their amplitudes are consistent with more traditional diagnostics.

[23] Providing this isothermal approximation $T(x, y, z) = T(x, y, 1\text{ km})$, the barometric equation eventually reduces to the Laplace formula, where $H(x, y) = \frac{RT}{g}$ is the atmospheric scale height,

$$P_{lev}(x,y) = e^{-\frac{z_{ref}-z(x,y)}{H(x,y)}} P(x,y). \quad (3)$$

[24] This formula is applied to each pixel (x, y) of the surface pressure field $P(x, y)$ retrieved for a given OMEGA session. Values of z are taken from the MOLA altimetry, and the value of z_{ref} is set to the mean altitude of the region under consideration. In the present paper, the amplitude of the topography on which we apply our correction is usually less than a few hundred meters, and reaches a maximum of 1919 m for the map displayed in Figure 11. Assuming, e.g., a 20 K overestimation of the scale height temperature, the error on the reduced pressure will be a moderate overestimation of about 2 and 7 Pa for a correction of 500 and 2000 m respectively.

3.3. Registration Shift Correction

[25] A first attempt to use the hydrostatic reduction formula on an OMEGA surface pressure map will suffer problems because the registration of the OMEGA data in the MOLA coordinate system is imperfect. The registration shift is usually below 2 pixels for large-scale sessions (64 and 128 scan pixels) and below 4 pixels for narrow sessions (16 and 32 scan pixels), which is small and usually not problematic for most studies based on the OMEGA data. However, since in the Laplace formula we combine the MOLA altimetry z and the OMEGA altimetry P, any registration shift will lead to features in the leveled surface pressure field P_{lev} with artificially high and low values positioned similarly at the border of all craters and mountains (Figure 4).

[26] The applied correction is based on the assumption of a constant two-dimensional misregistration. A "special"

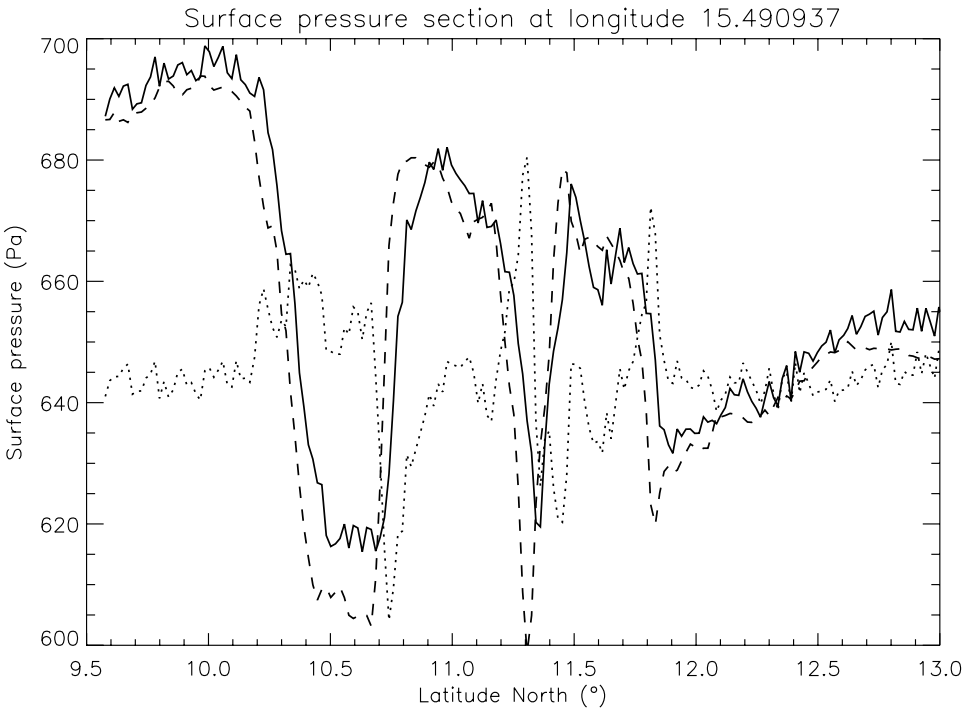

Figure 4. Meridional section of surface pressure fields in the ORB0278_3 case prior to any registration shift correction. The OMEGA surface pressure field (solid line) is slightly shifted from the reference surface pressure field based on MOLA (dashed line). As a result, the OMEGA leveled surface pressure field (dotted line) features artificial high/low values in the vicinity of the highest topographical gradients.

euclidian distance $d = \sqrt{(e^{P_{surf}} - e^{P_{ref}})^2}$ is used to ensure a correction mostly based on the well-defined orographic features (mountains and craters). To avoid unwanted smoothing due to the necessary re-interpolation step at the end of the correction process, we chose to shift the less noisy field (MOLA) with respect to the measured field (OMEGA). The resulting correction is found to be efficient in most cases, with no residual shift between the topographical features in both pressure fields (Figure 5). In the examined regions where topographical contrasts may be

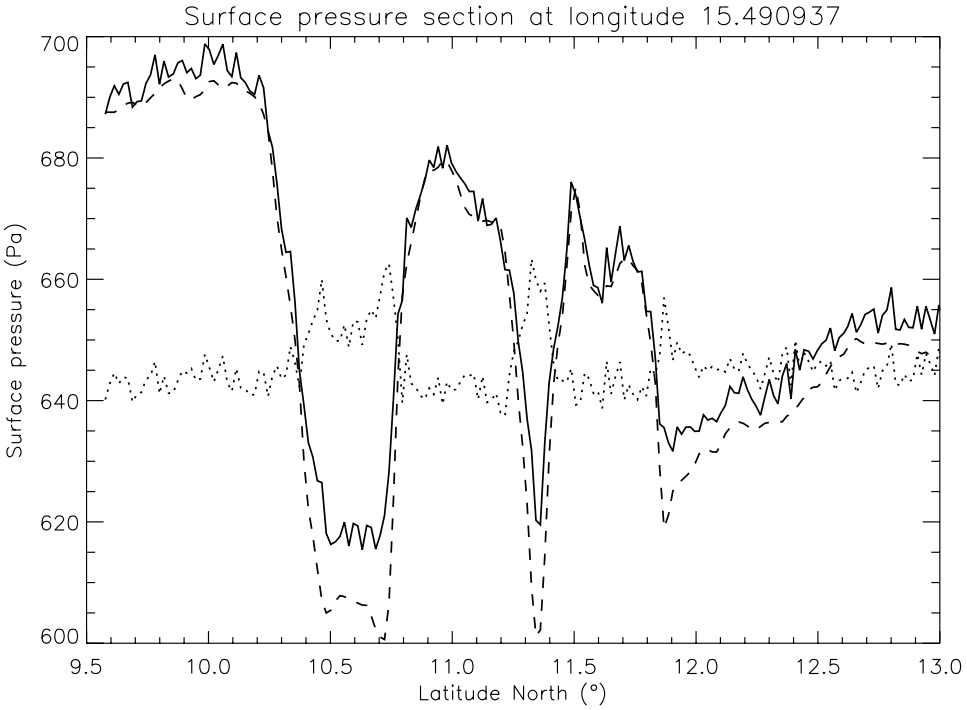

Figure 5. Same as Figure 4, after the registration shift correction.

high, as in the ORB0278_3 case, we perform sensitivity tests (with prescribed values of registration shift correction) to ensure that the observed structures in the leveled surface pressure field (see Figures 11 and 12 in the next section) do not arise artificially from the registration shift correction process. No dramatic change in the structure and the orientation of the identified features and only slight effects on their amplitudes were observed.

[27] The linear shift assumption is usually not valid over an entire OMEGA session, because of the internal deformation of the session geometry, especially near the borders of the large-scan orbits. Therefore we apply the registration shift correction only to selected areas within an OMEGA observation. The meteorological maps of this paper are thus focused on limited regions of given OMEGA observations.

4. Case Studies

[28] The present paper is based on particular case studies, each being representative of the types of pressure maps that can be built from the OMEGA data set: pressure gradients in flat areas, atmospheric oscillations, specific circulation around the Martian mountains and craters. Quality controls were performed in each case, and ruled out all the possible sources of bias in the pressure measurement process: specific low albedo features; poorly insolated region; shadowing effects near the topographical features; clouds, ground ice and dust pollution; observational artifacts; and registration shift correction artifacts. The limitations identified in the previous sections render the exploration of the OMEGA data set and the surface pressure measurements particularly non-systematic. After a preliminary selection of the seasons when the observation conditions should be favorable, the surface pressure retrieval was attempted for 65 OMEGA observations (chosen among the sessions acquired between January 2004 and November 2005). Further analysis showed that only 29 surface pressure measurements could be regarded as reliable. A completely automatized treatment of the whole OMEGA data set is thus beyond the scope of this paper: a more systematic and extensive analysis is left as future work.

4.1. Pressure Gradients

4.1.1. Observation

[29] This example is chosen in the Utopia Planitia region (east longitudes ranging from 95° to 97.5°, north latitudes ranging from 37° to 41°). The reference of the OMEGA cube is ORB0313_4, and the typical size of the map pixels is 4 × 4 km. This OMEGA observation took place at the beginning of the MY27 northern spring ($L_s \sim 20.8°$) and the local time is 10.8 Martian hours. The mean wind profile extracted from the Mars Climate Database for this area and season is not vertically uniform. A wind shear is predicted around 1 km: above this level, the wind velocity is nearly meridional and directed northward, while in the boundary layer the wind velocity is meridional too, but oriented southward.

[30] In this area, the topography is especially smooth. The terrain slope is, however, not negligible (~600 m), and its orientation is northeast–southwest (the highest point of the map is in the southwest corner). When the ''sea-level'' pressure reduction is applied to the raw surface pressure field, a purely meridional gradient is clearly revealed (Figure 6). The pressure gradient zonally extends over all the considered part of the ORB0313_4 observation. Leveled surface pressure is increasing northward; the amplitude of the meridional pressure variations is ~25 Pa over a distance of ~150 km (~3° latitude). Another example was available in the ORB0368_3 observation of an area close to the one considered here, although the surface pressure gradient was less clearly identified.

4.1.2. Discussion

[31] The example chosen here shows a well-organized surface pressure gradient observed over a localized region of 100–200 km extent. The leveled pressure gradient identified in the OMEGA data is also found on the Mars Climate Database pressure field, derived from GCM simulations. The orientation and the structure of the gradient is very similar in the two fields, but the pressure gradient on the GCM field is smoother, with a magnitude of only ~10 Pa over a distance of 150 km. The OMEGA pressure gradient is thus found to be more intense than the gradient predicted by the GCM.

[32] In the OMEGA surface temperature field, a well-organized nearly meridional positive gradient of ~10 K is detected. The GCM surface temperature gradient, extracted from the Mars Climate Database, displays the same direction, orientation and amplitude as the OMEGA one for this season and location. Therefore the surface temperature conditions in the selected area are very close to the GCM situation, in contrast to the surface pressure gradient. It is, however, possible on Mars, where radiative forcing dominates the surface energy budget, that an enhanced surface pressure gradient is identified in a region where no peculiar surface temperature disturbance is detected.

[33] The surface pressure diurnal cycle due to the thermal tide forcing is significant in this region at the beginning of the northern spring, and could thus explain the occurrence of such surface pressure gradients. However, the fact that the gradient is stronger in the observation may highlight an additional meteorological phenomenon not resolved at the GCM resolution. What is identified on the pressure field could then be the signature of an atmospheric front in the region, i.e., a localized (but possibly of large extent) temperature and/or pressure gradient that denotes a strong departure of the flow from the geostrophic balance. This assumption may be supported by the fact that Utopia Planitia is a region where, under specific conditions (mainly in fall and winter, but possibly in spring) frontal storms are known to move southward from the baroclinic storm track [*Wang et al.*, 2003]. Interestingly, we found that this OMEGA observation is located exactly in a region where the GCM predicts a local maximum of transient waves activity, with a day-to-day RMS pressure variability larger than 10 Pa (corresponding to peak-to-peak day-to-day variation of about 30 Pa). This can be compared to the maximum simulated activity in fall and winter which reaches 20 Pa RMS.

4.2. Atmospheric Oscillations

4.2.1. Observations

4.2.1.1. Case 1

[34] The first example chosen is in the Amazonis Planitia region (east longitudes ranging from 201° to 204°, north

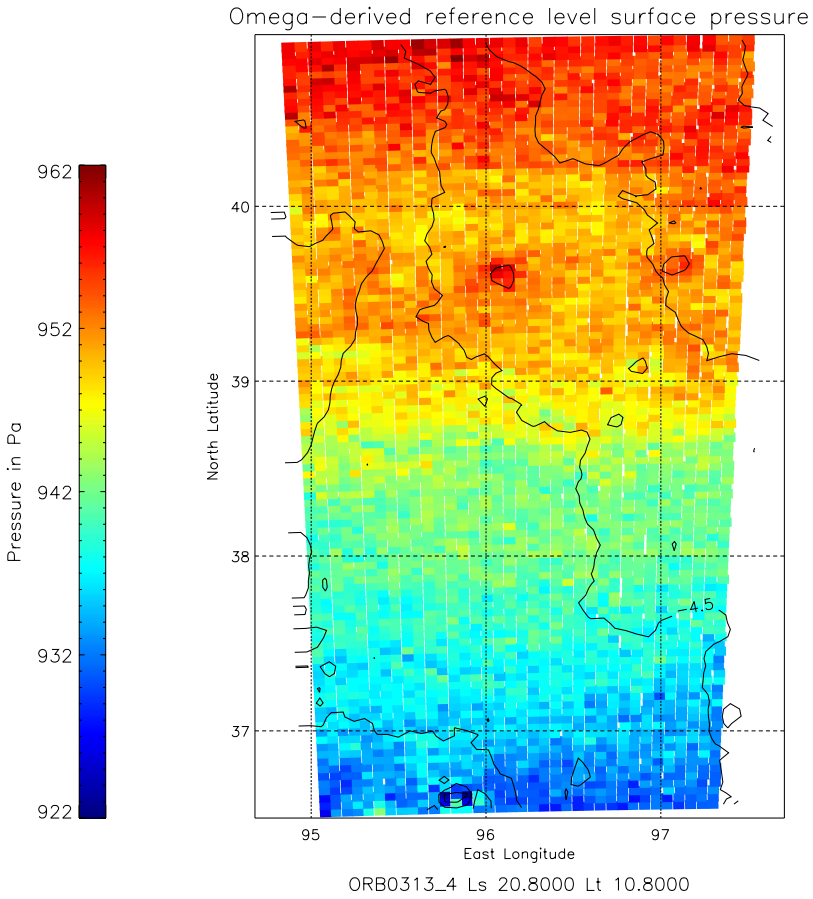

Figure 6. OMEGA surface pressure map in the Utopia Planitia region. The surface pressure field is hydrostatically reduced to a level of reference ("sea-level pressure reduction"). Contours stand for the topography, which is increasing ~600 m in the northeast direction.

latitudes ranging from 19° to 28°). The reference of the OMEGA cube is ORB0351_3, and the typical size of the map pixels is 2.3 × 2.3 km. This OMEGA observation took place at the beginning of the MY27 northern spring ($L_s \sim$ 26.4°) and the local time is 10 Martian hours. By the end of the morning, the predicted northward winds are usually rather strong at this season on these plains, and tend to bend eastward as they propagate northward.

[35] Well-defined surface pressure oscillations are directly detected in the raw surface pressure field (not shown). As the topography is very flat (Figure 7, left), the leveled surface pressure map (Figure 7, right) is very similar to the raw surface pressure map. The amplitude of the oscillations is ~10 Pa, above the instrumental noise limit. Surface pressure in the small craters of the considered area exhibits similar values in the OMEGA raw surface pressure map and in the prediction map, which indicates that the absolute pressure measurement on this OMEGA session is reliable. The morphology of the 2 μm band was checked in several pixels of the OMEGA map, and no anomaly was identified. Thus the oscillations are not related to any other pixel-to-pixel spectral variations than the CO_2 band depth variations.

[36] Therefore the observed oscillations seem to correspond to pressure oscillations. The horizontal wavelength is ~75 km. No oscillations are detected in the surface temperature field derived from the thermal part of the OMEGA spectra. The surface temperature is found to be particularly uniform over the whole region, and rather high (~260–270 K) in fair agreement with the Mars Climate Database prediction.

[37] An additional diagnostic can be obtained from the OMEGA data, and may be meaningful for the dynamical analysis of the oscillations detected. It is possible to draw (independently of any surface pressure diagnostic) maps of apparent ozone abundance above 20 km from the O_2 dayglow emission peak at 1.27 μm [*Fedorova et al.*, 2006; *Zasova et al.*, 2006]. In the ORB0351_3 ozone concentration map (F. Altieri, personal communication, 2006), periodic patterns are found, similar to those identified in the surface pressure map, but with a lower wavelength of ~50 km (Figure 8). Since ozone is usually considered as a dynamical tracer, the detected oscillations may be the signature of the same dynamical phenomenon as the one highlighted in the surface pressure map, at higher altitude.

4.2.1.2. Case 2

[38] The second example is selected in the Meridiani Terra region (east longitudes ranging from 24.75° to 25.25°, north latitudes ranging from −7° to −8°). The reference of the OMEGA cube is ORB1201_3, and the typical size of the map pixels is 1 × 1 km. This OMEGA

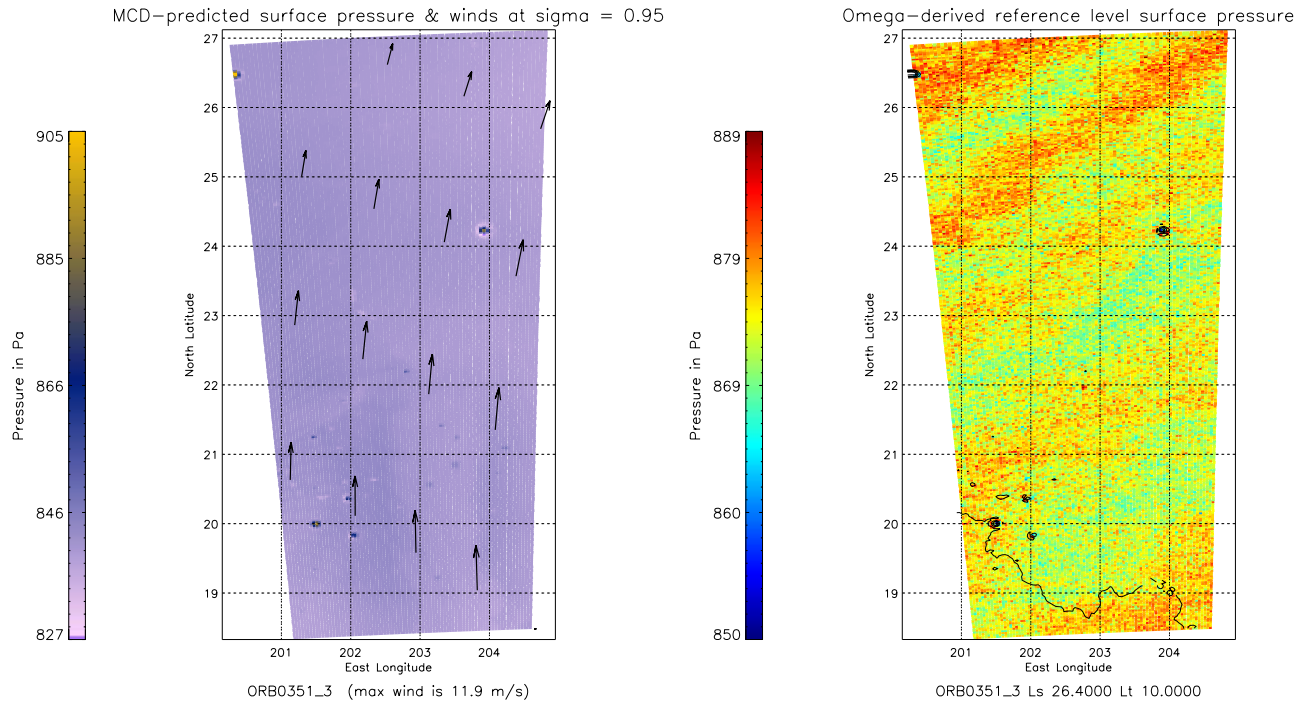

Figure 7. Surface pressure maps in the Amazonis Planitia region. (left) Prediction based on the MOLA topography. The vectors are the GCM-predicted winds around ∼1 km altitude, extracted from the Mars Climate Database v4.1. (right) OMEGA surface pressure field hydrostatically reduced to a level of reference ("sea-level pressure reduction").

observation took place at the end of the MY27 northern summer ($L_s \sim 133.9°$) and the local time is 12.5 Martian hours. The predicted wind is found to be small (maximum velocity <1.5 m.s^{-1}) in the area at this particular season and local time. However, reality might be different: a regional dust storm was detected on the ORB1212_3 OMEGA observation done 3 sols later and in the same region as the ORB1201_3 measurement (A. Määttänen, personal communication, 2006). The instantaneous local winds may thus be much stronger than the GCM wind predictions.

[39] The considered area is inside a large crater centered on 25E, −8N. The topography is rather flat: the only noticeable feature is a small hill in the center of the crater (Figure 9, left). The surface temperature is found to be particularly high, as in the first case.

[40] In this second case, a pressure oscillation pattern is identified northwest of the small central hill (Figure 9, right). Similar oscillations were found on the ORB0030_1 leveled surface pressure field, but the correlation with the topography was not ruled out rigourously enough to get a further insight in this example. The amplitude of the pressure oscillations is ∼30 Pa, above the instrumental noise limit. The horizontal wavelength is ∼6−10 km, clearly in the mesoscale dimension, unlike the previous case. Another major difference between the two cases is that no oscillations are detected in the ozone concentration map of this area.

4.2.2. Discussion

[41] Inertia-gravity waves are conspicuous atmospheric events in the Martian atmosphere [*Creasey et al.*, 2006]. In both cases, the identified oscillations on the surface pressure maps may be the signature of inertia-gravity waves. The horizontal wavelength of the oscillations in the first case is in the medium to high range for regular inertia-gravity waves on Mars [*Read and Lewis*, 2004]. The fact that similar oscillations are found in the ozone concentration field (with a different horizontal wavelength) might suggest the vertical propagation of the waves. In the second case, the horizontal wavelength is smaller, and no corresponding ozone oscillations are detected. This may suggest, according to the gravity wave dispersion relation, a more localized and faster wave event.

[42] Inertia-gravity waves can originate from strong convective motions in the atmosphere, or from a meteorological situation far from the geostrophic equilibrium (near-surface front or higher altitude jet-stream), as is the case on Earth [see, e.g., *Plougonven et al.*, 2003; *Vincent and Alexander*, 2000]. For example, the first case is located in an area of strong predicted wind curvature (Figure 10), which might indicate an extended unbalanced ageostrophic motion likely to emit gravity waves. Besides, in the two cases, the spring season is favorable to convective motions, which may also give rise to gravity waves. Interaction between mountains and winds is another mechanism to trigger such waves [*Pickersgill and Hunt*, 1981; *Tobie et al.*, 2003]. This source is more plausible in the second observation, chosen inside a large crater, than in the first observation, obtained in a zone of flat topography. However, in the first case, the influence of the high volcanoes east of the considered area cannot be ruled out, since the source of the waves may be found far from the area of gravity wave detection, especially in the case of slow gravity waves.

[43] Inertia-gravity waves are not the only oscillatory atmospheric phenomena which could explain the observa-

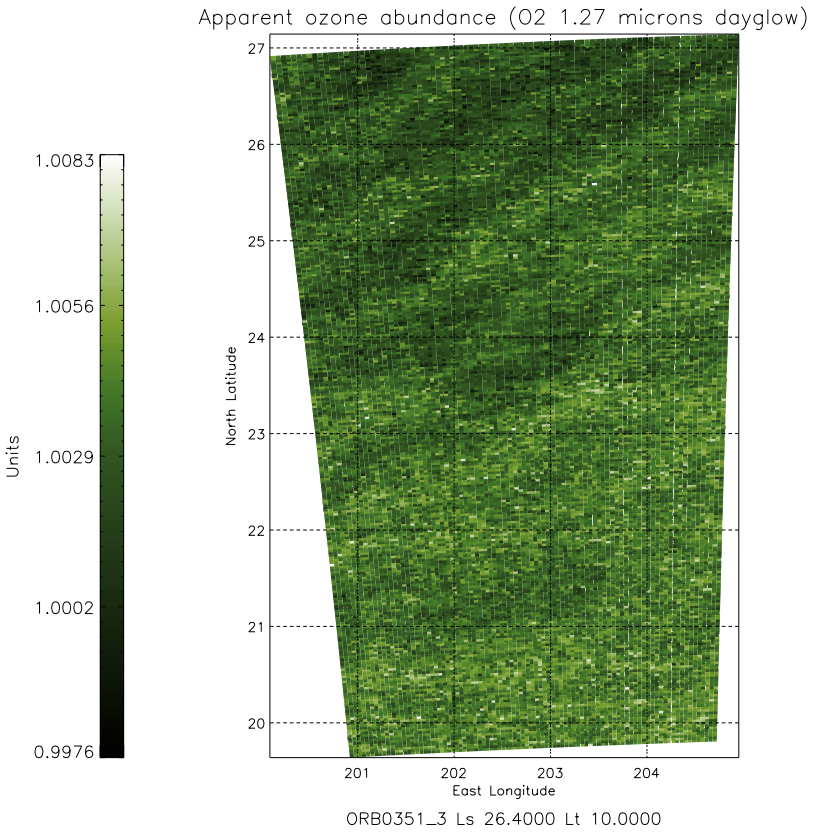

Figure 8. The 1.27 μm O_2 emission OMEGA map. The displayed variable is the ratio between the reflectance at 1.271 μm (O_2 emission) and the mean reflectance at 1.256 μm and 1.285 μm (continuum). This variable indicates the concentration of the passive tracer O_3 above 20 km. The method used in this map is described by *Zasova et al.* [2006] and was provided as a personal communication by F. Altieri (2006).

tion. An alternative explanation for the identified oscillations in the surface pressure field is the occurrence of horizontal convective rolls in the convective boundary layer (CBL). The horizontal rolls are generated by two general mechanisms which often act in concert: thermal instability (buoyancy accelerations of the atmosphere associated with a particularly hot surface) and dynamical instability (due to inflection points in the wind profiles). Upward and downward motions appear between the rolls, leading under favorable conditions to dust lifting or local clouds in the vicinity of the roll interstices [*Wang and Ingersoll*, 2002]. Signature of the convective rolls may also appear as oscillations on the surface pressure field.

[44] Examples of dry boundary layer convection on Earth are available in regions sharing great similarities with the Martian environment: e.g., the MATADOR measurement campaign in the arid Arizona desert [*Renno et al.*, 2004; J. Koch and N. O. Renno, Interactions between boundary layer convection, mineral dust and solar radiation, submitted to *J. Am. Sci.*, 2006]. The aspect ratio of observed rolls (i.e., wavelength over CBL depth) is on average $\sim$2 to 4, in good agreement with theoretical and observational references [*Young et al.*, 2002]. In case thermal risings perturb the CBL top (and penetrate into the stably stratified free atmosphere), gravity waves may be generated by a similar mechanism as the lee wave generation [*Stull*, 1976]. Under the influence of these gravity waves, "wide rolls" with aspect ratio between 5 and 9 may appear.

[45] Terrestrial and Martian convective roll structures are rather similar. We may, however, keep in mind two major differences: on Mars, the turbulent convection is more vigorous than on Earth (due to thinner atmosphere and reduced gravity), and its strength is predominantly related to the direct infrared radiative heating in the lowest levels of the CBL [*Michaels and Rafkin*, 2004]. As a result, the CBL on Mars experiences an explosive growth as the end of the morning approaches (around local time $\sim$11 h) and the CBL top may reach the maximum altitude of $\sim$10 km in the middle of the afternoon [*Rafkin et al.*, 2001].

[46] In the present paper, the convective roll explanation for the identified oscillations is plausible owing to the northern spring/summer insolation conditions, leading to a strong radiative forcing in the two cases. Given the mean aspect ratio of the widest rolls on Earth, and afternoon CBL height on Mars, convective rolls of wavelength $\sim$50 km to 90 km are likely to be found on Mars. Therefore, in the first case, the λ_H $\sim$75 km oscillations may be the signature of "wide rolls" modulated by jointly generated gravity waves. Without any gravity wave forcing, the occurrence of CBL-confined rolls with such a large horizontal wavelength would be rather impossible and the detected ozone oscillations at higher altitudes would not be accounted for.

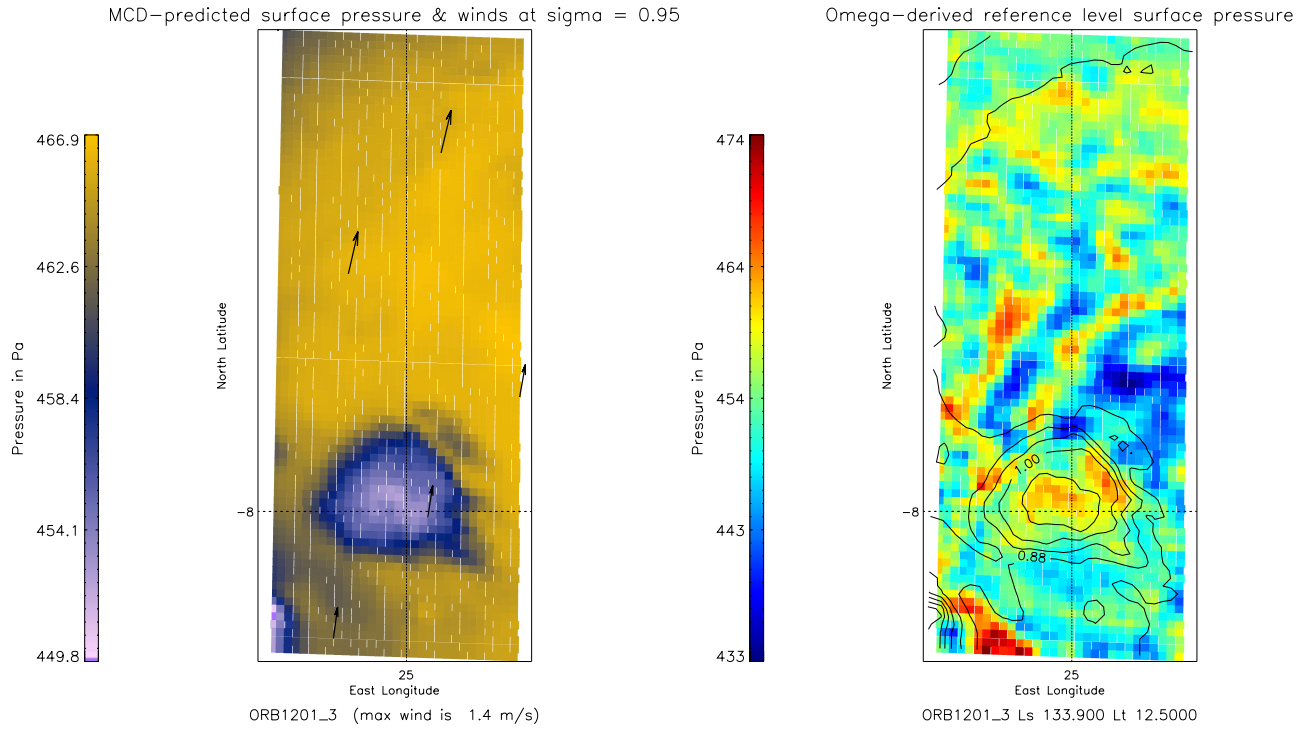

Figure 9. Surface pressure maps in the Meridiani Terra region. (left) Prediction based on the MOLA topography. The vectors are the GCM-predicted winds around ~1 km altitude, extracted from the Mars Climate Database v4.1. (right) OMEGA surface pressure field hydrostatically reduced to a level of reference ("sea-level pressure reduction"). Contours stand for the topography. The altimetry contrast between the highest and the lowest point of the map is ~200 m. Note: Due to low surface albedo (but not below the measurement limit of $A_L = 0.1$), the signal-to-noise ratio may be slightly lower than usual OMEGA observations. We thus choose to apply a 2 × 2 pixel window smoothing to the OMEGA field in this area. The main observed phenomena are not altered and are more clearly identified in the smoothed map, as the pixel-to-pixel contrast is decreased.

[47] In the second case, the oscillations are more likely to be the signature of purely thermally-driven or mechanically-driven convective rolls, with vertical extent limited to the CBL and no jointly generated gravity waves. This is consistent with the absence of oscillations in the ozone field above 20 km altitude. The case of simple convective rolls was modeled by *Rafkin et al.* [2001], using Large Eddy Simulations [see *Rafkin et al.*, 2001, Figure 14]. The horizontal convective rolls wavelength in the simulations at the beginning of the afternoon is ~3–5 km, which is close to the second case oscillations value. The horizontal structure of the rolls on the OMEGA ORB1201_3 map also shares similarities with the corresponding map in the *Rafkin et al.* [2001] article. However, several hours after sunrise, at the ORB1201_3 local time, the buoyancy-driven circulations may be dominant, and linear structures are no longer stable: convective updrafts and downdrafts tend to follow a polygonal organization [*Michaels and Rafkin*, 2004]. Therefore the linear structure highlighted in the second case must be maintained by a particularly strong wind in the region, which is plausible, as mentioned above, given the presence of a dust storm few days later. One question remains: why would the convective rolls exhibit stronger pressure signature than the more generalized polygonal structures that we do not observe in the OMEGA pressure maps?

4.3. Wind-Topography Interactions

4.3.1. Observations

4.3.1.1. Case 1

[48] A first example is chosen in Arabia Terra cratered terrains (east longitudes ranging from 15° to 16°, north latitudes ranging from 9.5° to 13.5°). The reference of the OMEGA cube is ORB0278_3, and the typical size of the map pixels is 1.5 × 1.5 km. This OMEGA observation took place at the beginning of the MY27 northern spring ($L_s \sim 15.6°$) and the local time is 11.7 Martian hours. The GCM-predicted wind, taken from the Mars Climate Database estimates, is blowing northward (and slightly westward) with an amplitude of ~7 $m.s^{-1}$ at 1 km altitude. The highest level of the selected area is very near the "zero datum" altitude on Mars ($P_s \sim 610$ Pa), and all the craters are ~2 km deep, except the northern one, less deep than the three others (Figure 11, left).

[49] Two main observations can be done on the resulting leveled surface pressure map (Figure 11, right). First, leveled surface pressure in the interior of craters is systematically 10 to 15 Pa lower than in the surrounding plains. Such low pressure values were observed in many craters in the OMEGA data set. Taking into account all possible artifacts, these low pressures seem to be real. In particular, an error on the atmospheric scale height used to reduce the

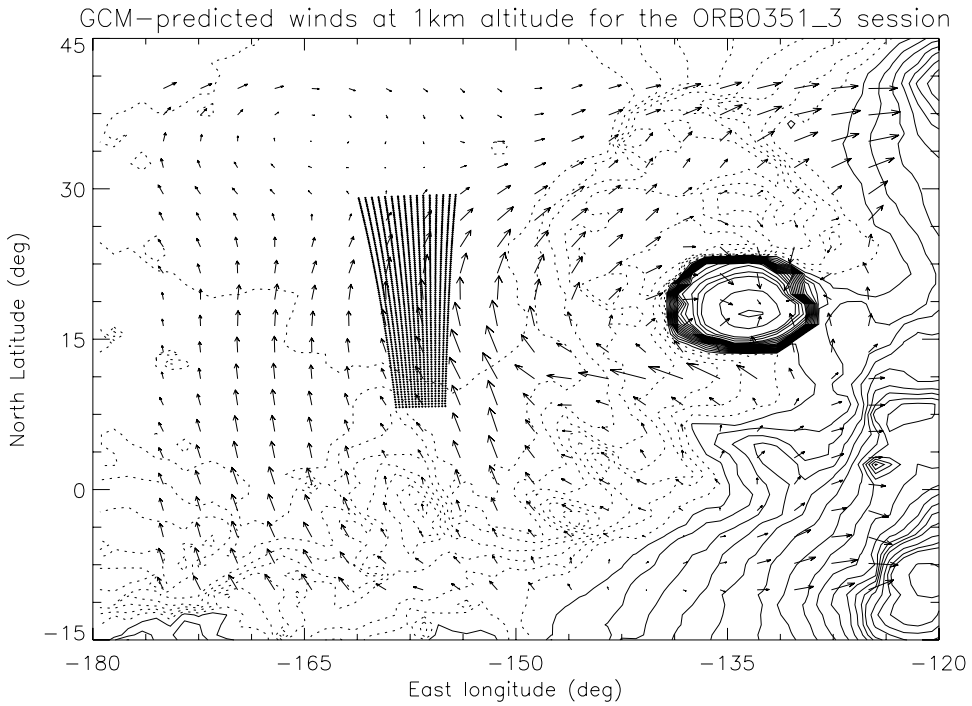

Figure 10. Extended latitude/longitude map of the Arabia Terra region where the ORB0351_3 measurement was carried out. The vectors are the GCM-predicted winds around ∼1 km altitude, extracted from the Mars Climate Database v4.1. Maximum velocity is 17.7 m.s^{-1}. Topography difference between two adjacent contours is 500 m.

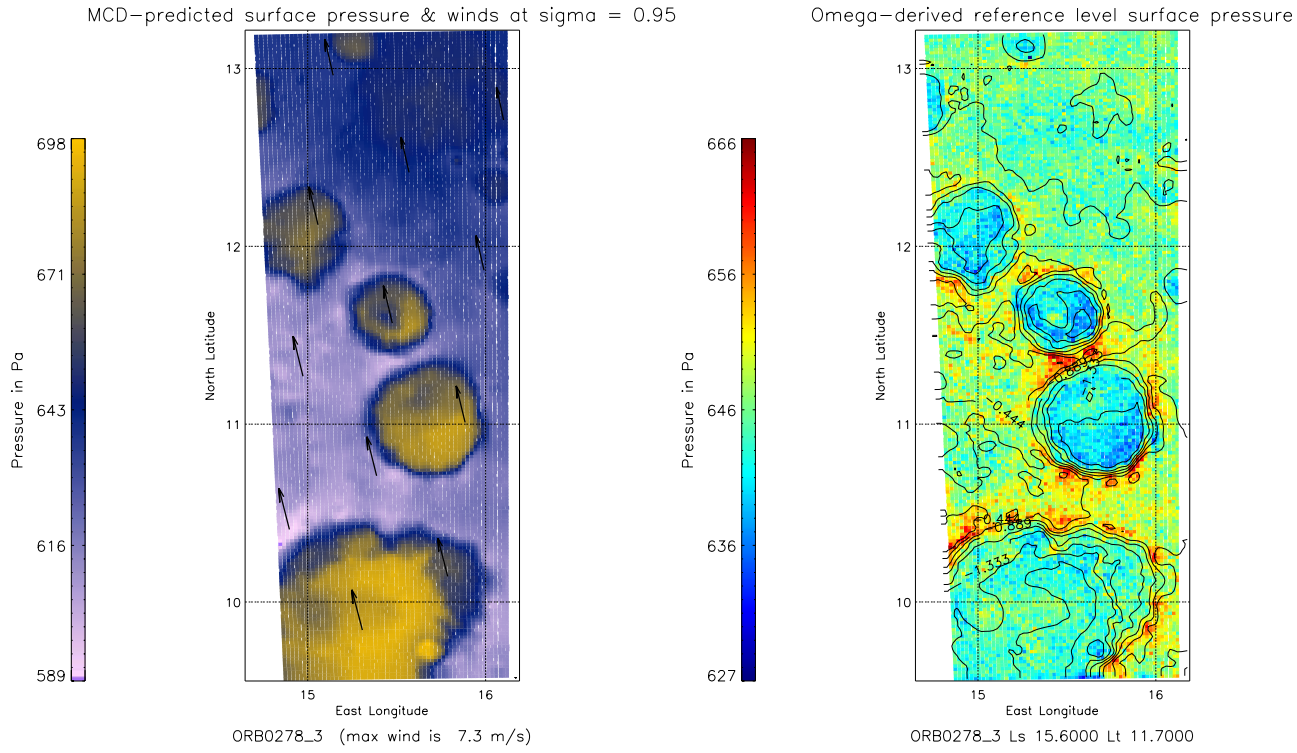

Figure 11. Surface pressure maps in the Arabia Terra region. (left) Prediction based on the MOLA topography. The vectors are the GCM-predicted winds around ∼1 km altitude, extracted from the Mars Climate Database v4.1. (right) OMEGA surface pressure field hydrostatically reduced to a level of reference ("sea-level pressure reduction"). Contours stand for the topography. The altimetry contrast between the highest and the lowest point of the map is ∼2 km.

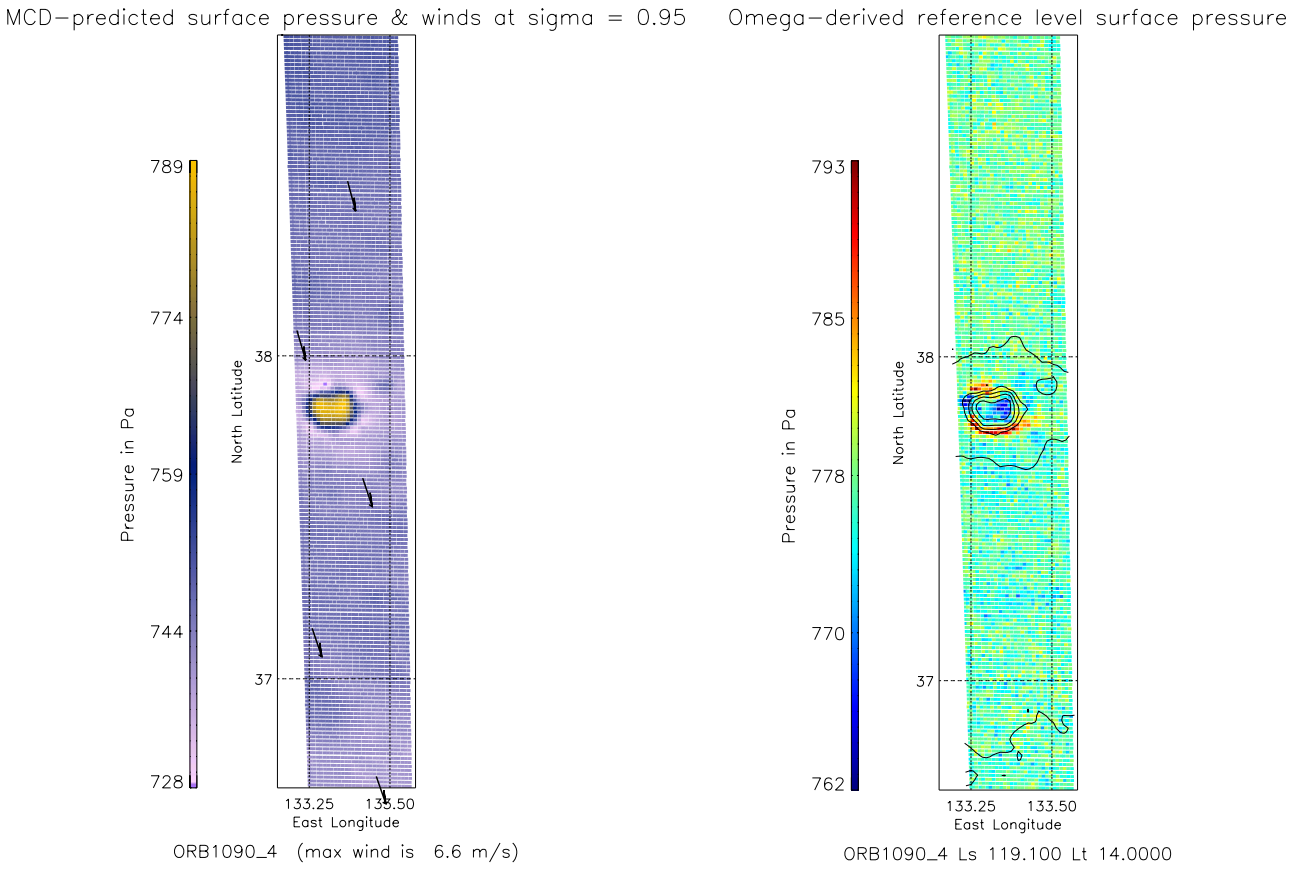

Figure 12. Surface pressure maps in the Utopia Planitia region. (left) Prediction based on the MOLA topography. The vectors are the GCM-predicted winds around ∼1 km altitude, extracted from the Mars Climate Database v4.1. (right) OMEGA surface pressure field hydrostatically reduced to a level of reference (“sea-level pressure reduction”). Contours stand for the topography. The altimetry contrast between the highest and the lowest point of the map is ∼1 km.

surface pressure to the reference level (see section 3) is not sufficient to explain the observed values. In the data processing, the scale height temperature is about 222 K. To increase the reduced pressure inside the crater up to the level observed outside the crater (1500 m above), one has to assume instead an impossible scale height temperature of 277 K, which is more than 40 K higher than the warmest near-surface temperature predicted in this area, and even higher than the surface temperatures observed by OMEGA and predicted in the Mars Climate Database.

[50] Secondly, local positive/negative pressure perturbations are identified in the vicinity of the crater rims. As was shown in section 4, the registration shift is corrected with great care, and the structures may not be correction artifacts. The orientation of the high/low pairs is mainly meridional. The pressure patterns and the incoming wind thus share the same north−south orientation.

4.3.1.2. Case 2

[51] The second example is an OMEGA observation obtained in Utopia Planitia with a narrow field-of-view (east longitudes ranging from 133.25° to 133.50°, north latitudes ranging from 37° to 39°). The reference of the OMEGA cube is ORB1090_4, and the typical size of the map pixels is 700 × 700 m. This OMEGA observation took place at the end of the MY27 northern summer (L_s ∼ 119.1°) and the local time is 14 Martian hours. The GCM-predicted wind, taken from the Mars Climate Database estimates, is blowing southward (and slightly eastward) with an amplitude of ∼6.6 m.s^{-1} at 1 km altitude.

[52] The topography of Utopia Planitia is usually very low and very flat. However, some sparse ejecta craters can be found in this region, and the present case features such an isolated crater ∼1 km deep (Figure 12, left).

[53] As can be seen in the leveled surface pressure map (Figure 12, right), this second case shares great similarities with the previous one. Similar positive-negative pressure perturbations are detected, with an amplitude of ∼30 Pa, and the orientation of these variations is identical to the GCM-predicted wind orientation. A higher pressure zone is detected on the windward rim of the crater. In the crater, a depression in surface pressure is detected. Another overpressure area is found on the leeward side of the topographical obstacle. The pressure perturbations are even more clearly identified as the crater is isolated, contrary to the previous case. Alternative cases very similar to the two examples displayed here were also found in other OMEGA sessions.

4.3.2. Discussion

[54] The existence of such large pressure gradients at such small scale is a surprising result which should be taken

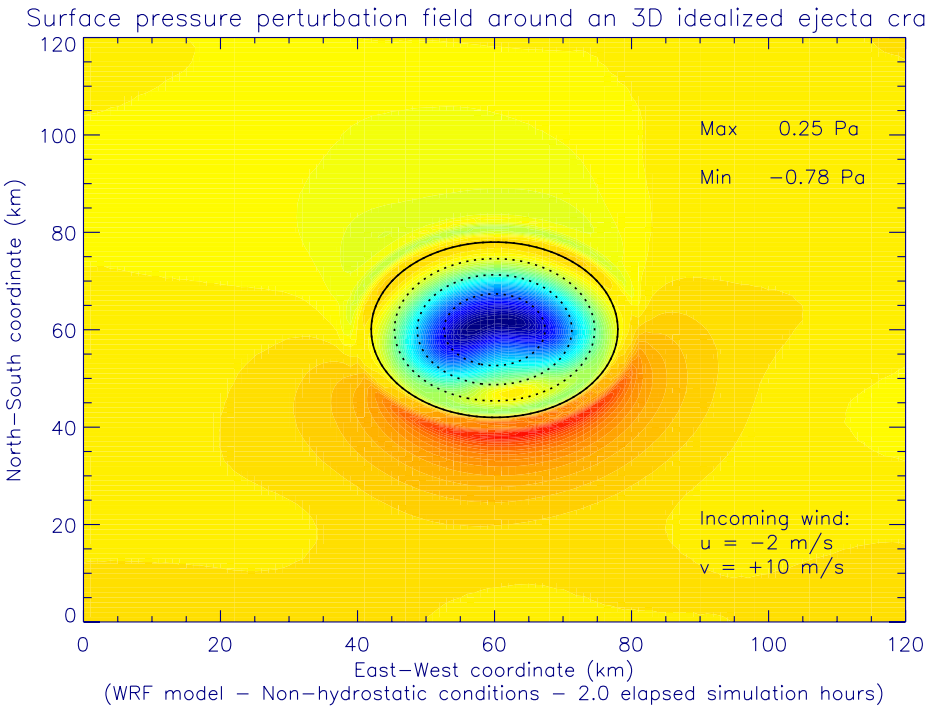

Figure 13. WRF "hill_2D" simulation adapted to the Martian conditions with the 3-D topographical obstacle defined in Appendix A. Surface pressure perturbation field after two elapsed simulation hours (equilibrium is reached). The incoming wind is northward and slightly westward. The mesoscale model is reduced to the dynamical solver. No physics packages are added. The horizontal resolution is 1 km, and the simulation time step is 5 s.

with caution. Nevertheless, the presence of localized highs and lows near the topographical gradients in the direction of the incoming wind is well documented on Earth [*Phillips*, 1984] and on Mars [*Pickersgill and Hunt*, 1981]. The classical result from linear theory, e.g., for an atmospheric flow impinging on a mountain, is an increase of surface pressure on the windward side of the mountain, where the flow is decelerated ("windward ridging") and a decrease of surface pressure on the leeward side, where the flow is accelerated ("leeward troughing") [*Smith*, 1980]. The situation for a Martian crater, a topographical depression circled by mountains, is, however, a bit more complicated. Nevertheless, in the displayed examples, the synoptic forcing (GCM-predicted wind direction) seems to be in accordance with the mesoscale pressure response (ridging and troughing in the vicinity of the obstacle).

[55] In general, the typical amplitude of the surface perturbation pressure p differ for various Rossby and Froude numbers [*Koffi et al.*, 1998]. A practical dimensionless parameter used in comparative studies is $Cp = \frac{p}{\rho NVH}$, where p is in Pa, ρ is the background mean air density in kg.m^{-3}, N is the buoyancy frequency in s^{-1}, H is the mountain height in m, and V is the modulus of the horizontal wind speed approaching the barrier in m.s^{-1}. ρ, N, H, V and p are the main parameters describing the purely dynamical interaction between the flow and the obstacle. Therefore, according to the laws of similitudes in fluid mechanics (Vaschy-Buckingham π theorem), we can assume that Cp values are similar on Earth and on Mars, which enables an estimation of the pressure perturbations in both cases. The Cp maximal values range from 0.4 to 2.5 [*Koffi et al.*, 1998], which leads to typical pressure perturbation values of ~0.6 hPa to 5 hPa on Earth ($\rho \sim$ 1.2 kg.m^{-3}, $N \sim$ 1.1 10^{-2} s^{-1}, H = 1500 m, and $V \sim$ 10 m.s^{-1}) and of 0.5 Pa to 4.5 Pa on Mars ($\rho \sim$ 0.02 kg.m^{-3} and $N \sim$0.6 10^{-2} s^{-1}, and H, V chosen as given previously). The terrestrial estimates are in rather good agreement with the measured values in the vicinity of real isolated mesoscale obstacles [*Mass and Ferber*, 1990; *Koffi et al.*, 1998]. The Martian estimates show that the detected perturbations on the OMEGA maps are probably too high in amplitude to be the signatures of a linear forcing of the synoptic flow upon a mesoscale barrier.

[56] The qualitative and quantitative analysis of the surface pressure signatures can be refined with the help of idealized non-hydrostatic 3-D numerical mesoscale simulations. Details about the simulations are given in Appendix A. Only the atmospheric mesoscale dynamics are taken into account: radiation, turbulence, ground friction are not included. The output displayed in Figure 13 was chosen after 2 elapsed hours of simulation, when the model has reached equilibrium. The structure of the surface pressure perturbations is rather close to the one described in the OMEGA maps, with a ridge in the vicinity of the windward rim and a trough inside the crater. The situation in the lee of the crater is a depression less deep than the one inside the crater, and a limited ridge is also identified in the lee of the crater. The perturbation pressure patterns identified in this simulation are thus qualitatively close to the ones displayed in the OMEGA meteorological maps. However, the simulated pressure perturbation amplitudes never exceed the 1 Pa limit, in good accordance with the linear theory estimates.

In the case of the wind velocity of $\sim$30 m.s^{-1} (not shown), the pressure perturbation amplitudes were also rather low (<4 Pa). It is thus unlikely that the surface pressure amplitudes found in the OMEGA maps ($\sim$10–15 Pa) are only due to the dynamical interaction between the crater and the incoming flow.

[57] Furthermore, mesoscale studies (more realistic than the highly idealized present simulations) clearly state that assumptions and generalizations based on large-scale average winds may lead to wrong mesometeorology diagnostics, especially in regions of complex topography [*Rafkin and Michaels*, 2003]. In such areas, non-hydrostatic motions and thermal forcings predominate, and resulting convection, turbulent motions and slope winds are dramatically vigorous. Since all the OMEGA measurements are made at the end of the morning or the beginning of the afternoon, the magnitude of non-hydrostatic slope winds is possibly high [*Savijärvi and Siili*, 1993; *Tyler et al.*, 2002]. The influence of these afternoon upslope katabatic winds, which result in air mass convergence in higher terrains, and air mass divergence in lower terrains, may explain the observed features near the rims of the craters, as the measured hydrostatic surface pressure is directly linked to the quantity of gas in the atmospheric column above a given pixel. In some OMEGA sessions (not shown here), the positive perturbation cells are more symmetrically spread around the craters, with no specific alignment with the GCM-predicted wind. The slope winds, and the resulting air divergence inside the crater and convergence at the rims, may explain these particularly symmetrical features. However, turbulent effects may also play a non-negligible role in the mesoscale circulation close to topographical obstacles, and even overwhelm the slope winds influence [*Rafkin et al.*, 2001].

5. Conclusion

5.1. Summary

[58] Surface pressure measurements help to achieve a better understanding of the main dynamical phenomena which occur in the atmosphere of a planet. The use of the Mars Express/OMEGA visible and near-IR imaging spectrometer allows us to achieve unprecedented remote sensing measurements of the Martian surface pressure. The OMEGA reflectances in the CO_2 absorption band at 2 μm are used to retrieve the surface pressure parameter, as described in the "part 1" paper by *Forget et al.* [2007]. The OMEGA surface pressure measurements are equivalent to atmospheric column mass measurements, results may therefore differ from barometric measurements at the surface of Mars, due to possible non-hydrostatic vertical motions. The measurement accuracy was found to be sufficient enough to allow a meteorological application for the resulting surface pressure maps.

[59] A preliminary selection of the OMEGA sessions has to be performed in order to ensure the reliability of the surface pressure retrieval. Basic limitations of the inversion algorithm performance are first checked for insufficient insolation, low albedo regions and saturation effects. Other parts of the OMEGA spectra are then used to assess carefully the presence of ices in the atmosphere (clouds) and on the surface (frosts), and to monitor the possible zones of local dust loading in the atmosphere.

[60] The topographical first-order influence is removed from the surface pressure field as on Earth, using a "sea-level" pressure reduction. This process is nothing more than a normalization, using the barometric equation, of all the pressure measurements made at various locations (and consequently at various altitudes). We use a constant scale height defined with the 1 km temperature, high enough above the slope wind layer, but low enough to keep the consistency of the barometric integration. Mountain and crater positions were found to be slightly shifted in the OMEGA pressure field, compared to the reference field derived from MOLA. Thus registration shift correction is performed prior to any topography removal process. Once the misregistration is corrected, leveled surface pressure maps are ready to be displayed for meteorological analysis. Three main phenomena are observed in the maps produced: horizontal pressure gradients, atmospheric oscillations, and pressure perturbations around the topographical obstacles.

[61] First, an example of an horizontal pressure gradient over a specific region is displayed. The gradient shares the same direction as the GCM-predicted gradient, but its amplitude is higher. As a result, this pressure gradient may be the signature of an atmospheric front occurring in the region. A possible influence of the pressure tide maximum is, however, not ruled out.

[62] Secondly, atmospheric oscillations are clearly detected in the OMEGA surface pressure fields. A first example featured a $\lambda_H \sim 75$ km wavelength oscillation event, whereas the oscillations in the second example were of smaller extent: $\lambda_H \sim 6$–10 km. These well-organized atmospheric oscillations may be the signatures of inertia-gravity waves and/or convective rolls. Atmospheric conditions in both cases are favorable to inertia-gravity waves emission. In the first case, similar oscillations are found in the ozone abundance field above 20 km altitude, but with a lower wavelength, which possibly suggests the vertical propagation of the oscillatory event. The horizontal wavelength of the pressure perturbations is also in reasonably good agreement with terrestrial estimates of dry convective rolls occurring in arid deserts (taking into account the higher Martian boundary layer top). In this case, the two phenomena, waves and rolls, may be coupled. In the second case, the horizontal wavelength is consistent with the mesoscale model predictions for convective roll motions.

[63] Thirdly, two examples of high/low surface perturbations in the vicinity of craters are displayed. Low pressure perturbations are also found within the craters. As the alignment of the perturbation cells is very similar to the predicted wind direction, an attractive assumption is that these cells are signatures of the interactions between the incoming flow and the craters. Using previous studies diagnostics and highly idealized mesoscale simulations (with an adapted version of the Weather Research Forecast model), the OMEGA surface pressure signatures in the vicinity of the craters are explained qualitatively but not quantitatively. Discrepancies may be a result of the drastic mesoscale circulation occurring in areas where the topography is particularly complex. Non-hydrostatic dynamics may play a dominant role: gravity waves, thermal forcings, slope winds, turbulent motions. In particular, the resulting mass divergence from inside the crater due to slope winds might also explain some of the observed features.

5.2. Perspectives

[64] The surface pressure maps reveal interesting signatures of meteorological events. Exhaustive interpretations of the identified structures are beyond the scope of this paper: the plausible explanations proposed in the case studies are very preliminary. It is worth reminding that, at the time of writing of this paper, remote-sensing pressure measurement on Earth are still very difficult to obtain. Thus interpretations of the structures revealed in the OMEGA surface pressure maps can hardly be compared to any terrestrial equivalent.

[65] The purpose of this paper and the companion paper is to show that the surface pressure measurement with OMEGA is difficult but feasible, and may lead to interesting meteorological diagnostics. The analysis of the OMEGA maps was performed on a few examples chosen among the numerous OMEGA sessions available. An extensive treatment of the complete data set was beyond the scope of this paper. It is, however, highly desirable and is left as future work. It might also be possible to apply this retrieval technique to the Compact Reconnaissance Imaging Spectrometer for Mars (CRISM) data.

[66] Similarly, ground-based telescopes may be valuable tools to map surface pressure across an entire hemisphere [*Chamberlain et al.*, 2006]. Such a technique requires difficult corrections, but can offer high-resolution spectral data in the CO_2 absorption band at 2 μm for the pressure retrieval. Maps repeatedly acquired at neighboring dates for the same hemisphere would be valuable tools to monitor the temporal evolution of baroclinic waves, which was difficult with the OMEGA data set.

[67] The OMEGA surface pressure maps provide new qualitative and quantitative inputs for meteorological models. Further analysis of the OMEGA surface pressure maps also requires high-resolution mesoscale modeling, where the main dynamical solver has to be coupled with the most realistic and exhaustive models of Martian environmental physics.

Appendix A: WRF Idealized Simulations

[68] To analyze more precisely the interaction between flow and topography, three-dimensional non-hydrostatic fully compressible idealized simulations were performed with the mesoscale Weather Research Forecast (WRF) model version 2.1.2 [*Skamarock et al.*, 2005]. In these highly idealized WRF simulations, only the atmospheric mesoscale dynamics are taken into account: radiation, turbulence, ground friction are not included. The basic WRF "hill_2D" idealized case is adapted to the Martian atmospheric parameters, with a 3-D topographical obstacle. The following relation defined the 3-D idealized crater altimetry, with $\rho = \sqrt{x^2 + y^2}$ in km, H and δ being respectively the depth and a width factor of the crater:

$$h(x,y) = H - \frac{1}{7500}\frac{H}{\delta^4} \times (\rho + 6\delta)(\rho - 6\delta)(\rho + 10\delta)(\rho - 10\delta) \times [\tanh(\rho + 7\delta) - \tanh(\rho - 7\delta)] \quad \text{(A1)}$$

[69] This formula, based on a fourth-order polynomial and a hyperbolic tangent attenuation factor, is a good approximation to a typical ejecta crater morphology. In the simulation of the present paper, the crater is defined by H = 2000 m and δ = 3 km. The morphology of the idealized crater is close to the topographical features of the ORB0278_3 OMEGA observation.

[70] The model was initialized to typical Martian atmosphere predicted for the ORB0278_3 conditions by the Mars Climate Database. The incoming wind is prescribed to be northward, nearly meridional and with amplitude $\sim$11 m.s^{-1}. Boundary conditions are opened, and spurious waves are damped at the borders and at the top of the domain. The horizontal resolution is set to 1 km, and the domain features 120 grid points in the north–south and east–west axis. 60 vertical hydrostatic pressure coordinates [*Laprise*, 1992] are set between 0 and 50 km. Time step is 5 s, which is in accordance with the CFL condition requirements for the WRF dynamical scheme, given the spatial resolution of 1 km. Simulations were run for 10 model hours.

[71] **Acknowledgments.** We wish to thank F. Altieri, P. Drobinski, J. P. Huot, D. Jouglet, F. Lott, A. Määttänen, F. Montmessin, N. Renno, and A. Simpson for invaluable discussions about the pressure maps. We also thank E. Millour, L. Montabone, L. Thevenard, and S. R. Lewis for helping us with careful proofreading of the manuscript. We are grateful to the entire Mars Express project and support teams for their tireless efforts at obtaining the data analyzed here and to the whole OMEGA science team for valuable discussions and comments. A part of this work was performed while F. Forget and B. Dolla were visiting the Space Science Division of NASA Ames Research Center (F.F. as a Senior National Research Council fellow). We wish to thank in particular R. M. Haberle along with G. Gibert, J. Hollingsworth, J. Schaeffer, T. Colaprete, and C. P. McKay for their support and advice. Finally, we thank S. Rodin and an anonymous reviewer for careful reviews and insightful comments which greatly improved the paper.

References

Bellucci, G., F. Altieri, J. P. Bibring, G. Bonello, Y. Langevin, B. Gondet, and F. Poulet (2006), OMEGA/Mars Express: Visual channel performances and data reduction techniques, *Planet. Space Sci.*, *54*, 675–684.

Bibring, J.-P., et al. (1991), Topography of the Martian tropical regions with ISM, *Planet. Space Sci.*, *39*, 225–236.

Bibring, J.-P., et al. (2004), OMEGA: Observatoire pour la Minéralogie, l'Eau, les Glaces et l'Activité, in *Mars Express: The Scientific Payload*, edited by A. Wilson, *Eur. Space Agency Spec. Publ.*, *ESA-1240*, 37–49.

Bibring, J.-P., et al. (2005), Mars surface diversity as revealed by the OMEGA/Mars Express observations, *Science*, *307*, 1576–1581.

Bösch, H., et al. (2006), Space-based near-infrared CO_2 measurements: Testing the Orbiting Carbon Observatory retrieval algorithm and validation concept using SCIAMACHY observations over Park Falls, Wisconsin, *J. Geophys. Res.*, *111*, D23302, doi:10.1029/2006JD007080.

Buchwitz, M., et al. (2006), Atmospheric carbon gases retrieved from SCIAMACHY by WFM-DOAS: Version 0.5 CO and CH_4 and impact of calibration improvements on CO_2 retrieval, *Atmos. Chem. Phys.*, *6*, 2727–2751.

Chamberlain, S., J. Bailey, M. Walter, A. Simpson, and D. Crisp (2006), Topographic and atmospheric pressure mapping using near infrared imaging and spectral observations of Mars, paper presented at Second Workshop on Mars Atmosphere Modelling and Observations, Cent. Natl. d'Etudes Spatiales, Granada, Spain.

Creasey, J. E., J. M. Forbes, and D. P. Hinson (2006), Global and seasonal distribution of gravity wave activity in Mars' lower atmosphere derived from MGS radio occultation data, *Geophys. Res. Lett.*, *33*, L01803, doi:10.1029/2005GL024037.

Dubuisson, P., R. Borde, C. Schmechtig, and R. Santer (2001), Surface pressure estimates from satellite data in the oxygen A-band: Applications to the MOS sensor over land, *J. Geophys. Res.*, *106*, 27,277–27,286.

Fedorova, A., O. Korablev, S. Perrier, J.-L. Bertaux, F. Lefevre, and A. Rodin (2006), Observation of O_2 1.27 μm dayglow by SPICAM IR: Seasonal distribution for the first Martian year of Mars Express, *J. Geophys. Res.*, *111*, E09S07, doi:10.1029/2006JE002694.

Forget, F., et al. (2006), The new Mars climate database, paper presented at Second Workshop on Mars Atmosphere Modelling and Observations, Cent. Natl. d'Etudes Spatiales, Granada, Spain.

Forget, F., A. Spiga, B. Dolla, S. Vinatier, R. Melchiorri, P. Drossart, A. Gendrin, J.-P. Bibring, Y. Langevin, and B. Gondet (2007), Remote sensing of surface pressure on Mars with the Mars Express/OMEGA spectrometer: 1. Retrieval method, *J. Geophys. Res.*, doi:10.1029/2006JE002871, in press.

Fournier, N., P. Stammes, M. de Graaf, R. van der A, A. Piters, M. Grzegorski, and A. Kokhanovsky (2006), Improving cloud information over deserts from SCIAMACHY oxygen A-band measurements, *Atmos. Chem. Phys.*, *6*, 163–172.

Gendrin, A., S. Erard, P. Drossart, and R. Melchiorri (2003), Observation of pressure variations in the Martian atmosphere, *Geophys. Res. Lett.*, *30*(23), 2227, doi:10.1029/2003GL018234.

Gondet, B., J.-P. Bibring, Y. Langevin, F. Poulet, F. Montmessin, and F. Forget (2006), One Martian year observation of H_2O ice clouds By OMEGA/Mars Express, paper presented at Second Workshop on Mars Atmosphere Modelling and Observations, Cent. Natl. d'Etudes Spatiales, Granada, Spain.

Gray, L. D. (1966), Transmission of the atmosphere of Mars in the region of 2 μ, *Icarus*, *5*, 390–398.

Hess, S. L., J. A. Ryan, J. E. Tillman, R. M. Henry, and C. B. Leovy (1980), The annual cycle of pressure on Mars measured by Viking landers 1 and 2, *Geophys. Res. Lett.*, *7*, 197–200.

Janjic, Z. I., J. P. Gerrity Jr., and S. Nickovic (2001), An alternative approach to nonhydrostatic modeling, *Mon. Weather Rev.*, *129*, 1129–1178.

Jouglet, D., F. Poulet, R. E. Milliken, J. F. Mustard, J.-P. Bibring, Y. Langevin, B. Gondet, and C. Gomez (2007), Hydration state of the Martian surface as seen by Mars Express OMEGA: 1. Analysis of the 3 μm hydration feature, *J. Geophys. Res.*, doi:10.1029/2006JE002846, in press.

Koffi, E., B. Bénech, J. Stein, and B. Terliuc (1998), Dynamic characteristics of regional flows around the Pyrénées in view of the PYREX Experiment. Part II: Solution of a linear model compared to field measurements, *J. Appl. Meteorol.*, *37*, 53–71.

Langevin, Y. (2005), OMEGA software documentation version 3, Inst. d'Astrophys. Spatiale, Orsay, France.

Langevin, Y., F. Poulet, J.-P. Bibring, B. Schmitt, S. Douté, and B. Gondet (2005), Summer evolution of the north polar cap of Mars as observed by OMEGA/Mars Express, *Science*, *307*, 1581–1584.

Laprise, R. (1992), The Euler equations of motion with hydrostatic pressure as an independent variable, *Mon. Weather Rev.*, *120*, 197–207.

Mass, C. F., and G. K. Ferber (1990), Surface pressure perturbations produced by an isolated mesoscale topographic barrier. Part I: General characteristics and dynamics, *Mon. Weather Rev.*, *118*, 2579–2595.

Melchiorri, R., P. Drossart, T. Fouchet, B. Bézard, F. Forget, A. Gendrin, J. P. Bibring, N. Manaud, and OMEGA Team (2006), A simulation of the OMEGA/Mars Express observations: Analysis of the atmospheric contribution, *Planet. Space Sci.*, *54*, 774–783, doi:10.1016/j.pss.2006.04.014.

Michaels, T. I., and S. C. R. Rafkin (2004), Large-eddy simulation of atmospheric convection on Mars, *Q. J. R. Meteorol. Soc.*, *130*(599), 1251–1274.

Michaels, T. I., A. Colaprete, and S. C. R. Rafkin (2006), Significant vertical water transport by mountain-induced circulations on Mars, *Geophys. Res. Lett.*, *33*, L16201, doi:10.1029/2006GL026562.

Mitchell, R. M., and D. M. O'Brien (1987), Error estimates for passive satellite measurement of surface pressure using absorption in the A band of oxygen, *J. Atmos. Sci.*, *44*, 1981–1990.

Phillips, S. P. (1984), Analytical surface pressure and drag for linear hydrostatic flow over three-dimensional elliptical mountains, *J. Atmos. Sci.*, *41*, 1073–1084.

Pickersgill, A. O., and G. E. Hunt (1981), An examination of the formation of linear lee waves generated by giant Martian volcanoes, *J. Atmos. Sci.*, *38*, 40–51.

Plougonven, R., H. Teitelbaum, and V. Zeitlin (2003), Inertia gravity wave generation by the tropospheric midlatitude jet as given by the Fronts and Atlantic Storm-Track Experiment radio soundings, *J. Geophys. Res.*, *108*(D21), 4686, doi:10.1029/2003JD003535.

Rafkin, S. C. R., and T. I. Michaels (2003), Meteorological predictions for 2003 Mars Exploration Rover high-priority landing sites, *J. Geophys. Res.*, *108*(E12), 8091, doi:10.1029/2002JE002027.

Rafkin, S. C. R., R. M. Haberle, and T. I. Michaels (2001), The Mars Regional Atmospheric Modeling System: Model description and selected simulations, *Icarus*, *151*, 228–256.

Rafkin, S. C. R., M. R. V. Sta. Maria, and T. I. Michaels (2002), Simulation of the atmospheric thermal circulation of a Martian volcano using a mesoscale numerical model, *Nature*, *419*, 697–699.

Read, P. L., and S. R. Lewis (2004), *The Martian Climate Revisited: Atmosphere and Environment of a Desert Planet*, Springer, New York.

Renno, N. O., et al. (2004), MATADOR 2002: A pilot field experiment on convective plumes and dust devils, *J. Geophys. Res.*, *109*, E07001, doi:10.1029/2003JE002219.

Rosenqvist, J. (1991), Mars: Etude de son atmosphère par le spectro-imageur ISM, Ph.D. thesis, Université Paris 7, Paris.

Savijärvi, H., and T. Siili (1993), The Martian slope and the nocturnal PBL jet, *J. Atmos. Sci.*, *50*, 77–88.

Schofield, J. T., D. Crisp, J. R. Barnes, R. M. Haberle, J. A. Magalhaães, J. R. Murphy, A. Seiff, S. Larsen, and G. Wilson (1997), The Mars Pathfinder Atmospheric Structure Investigation/Meteorology (ASI/MET) experiment, *Science*, *278*, 1752–1757.

Skamarock, W. C., J. B. Klemp, J. Dudhia, D. O. Gill, D. M. Barker, W. Wang, and J. G. Powers (2005), A description of the Advanced Research WRF, version 2, technical note, Natl. Cent. for Atmost. Res., Boulder, Colo.

Smith, D. E., et al. (2001), Mars Orbiter Laser Altimeter: Experiment summary after the first year of global mapping of Mars, *J. Geophys. Res.*, *106*, 23,689–23,722.

Smith, M. D. (2006), TES atmospheric temperature, aerosol optical depth, and water vapor observations 1999–2004, paper presented at Second Workshop on Mars Atmosphere Modelling and Observations, Cent. Natl. d'Etudes Spatiales, Granada, Spain.

Smith, R. B. (1980), Linear theory of stratified hydrostatic flow past an isolated mountain, *Tellus*, *32*, 348–364.

Stull, R. B. (1976), Internal gravity waves generated by penetrative convection, *J. Atmos. Sci.*, *33*, 1279–1286.

Tobie, G., F. Forget, and F. Lott (2003), Numerical simulation of the winter polar wave clouds observed by Mars Global Surveyor Mars Orbiter Laser Altimeter, *Icarus*, *164*, 33–49.

Toigo, A. D., and M. I. Richardson (2003), Meteorology of proposed Mars Exploration Rover landing sites, *J. Geophys. Res.*, *108*(E12), 8092, doi:10.1029/2003JE002064.

Tyler, D., Jr., J. R. Barnes, and R. M. Haberle (2002), Simulation of surface meteorology at the Pathfinder and VL1 sites using a Mars mesoscale model, *J. Geophys. Res.*, *107*(E4), 5018, doi:10.1029/2001JE001618.

Vincent, R. A., and M. J. Alexander (2000), Gravity waves in the tropical lower stratosphere: An observational study of seasonal and interannual variability, *J. Geophys. Res.*, *105*, 17,971–17,982.

Wang, H., and A. P. Ingersoll (2002), Martian clouds observed by Mars Global Surveyor Mars Orbiter Camera, *J. Geophys. Res.*, *107*(E10), 5078, doi:10.1029/2001JE001815.

Wang, H., M. I. Richardson, R. J. Wilson, A. P. Ingersoll, A. D. Toigo, and R. W. Zurek (2003), Cyclones, tides, and the origin of a cross-equatorial dust storm on Mars, *Geophys. Res. Lett.*, *30*(9), 1488, doi:10.1029/2002GL016828.

Young, G. S., D. A. R. Kristovich, M. R. Hjelmfelt, and R. C. Foster (2002), Rolls, streets, waves, and more: A review of quasi-two-dimensional structures in the atmospheric boundary layer, *Bull. Am. Meteorol. Soc.*, *83*, 997–1001.

Zasova, L. V., et al. (2006), Ozone in Martian atmosphere from the 1.27 μm O_2 emission: OMEGA/Mars Express measurements, paper presented at Second Workshop on Mars Atmosphere Modelling and Observations, Cent. Natl. d'Etudes Spatiales, Granada, Spain.

B. Dolla, F. Forget, and A. Spiga, Laboratoire de Météorologie Dynamique, CNRS-UPMC BP99, 4 Place Jussieu, F-75252 Paris Cedex 05, France. (forget@lmd.jussieu.fr; spiga@lmd.jussieu.fr)

P. Drossart, R. Melchiorri, and S. Vinatier, LESIA Observatoire de Paris-Meudon, 5 Place Jules Janssen, F-92195 Meudon Cedex, France.

J.-P. Bibring, A. Gendrin, B. Gondet, and Y. Langevin, Institut d'Astrophysique Spatiale, Bâtiment 121, Université Paris Sud 11, F-91405 Orsay Cedex, France.